Available online at www.sciencedirect.com
ScienceDirect
Ceramics International 37 (2011) 1895–1904
CERAMICS INTERNATIONAL
www.elsevier.com/locate/ceramint

Mechanochemical synthesis of $Ti_{1-x}Zr_xB_2$ and $Ti_{1-x}Hf_xB_2$ solid solutions

M.A. Avilés, J.M. Córdoba, M.J. Sayagués, F.J. Gotor *

Instituto de Ciencia de Materiales de Sevilla (CSIC-US), Américo Vespucio 49, 41092 Sevilla, Spain

Received 10 January 2011; received in revised form 9 February 2011; accepted 11 February 2011
Available online 19 February 2011

Abstract

Solid solutions of TiB_2–ZrB_2 and TiB_2–HfB_2 were obtained under an inert atmosphere by high-energy ball-milling mixtures of Ti/Zr/B and Ti/Hf/B, respectively. Milling promoted mechanically induced self-sustaining reactions (MSR), and the ignition time was dependent on the initial composition of the mixture. The stoichiometry of $Ti_{1-x}Zr_xB_2$ and $Ti_{1-x}Hf_xB_2$ solid solutions was controlled by adjusting the atomic ratio of the reactants. The solid solutions were characterised by X-ray diffraction, transmission electron microscopy, electron diffraction, and energy dispersive X-ray spectroscopy. The results revealed that TiB_2–ZrB_2 possessed a nanometric microstructure and good chemical homogeneity. However, in the TiB_2–HfB_2 system, an inhomogeneous solid solution was obtained when a Ti-rich mixture was employed. The solid solutions showed good thermal stability; thus, can be used as raw materials for the development of technological materials for structural applications.

Keywords: A. Milling; B. X-ray methods; D. Borides; E. Structural applications

1. Introduction

Diborides of group IVB transition metals (TiB_2, ZrB_2, and HfB_2) are useful compounds for the development of advanced materials for high-temperature technological applications because these compounds display high melting points (greater than 3000 °C), high hardness and strength at high temperatures, good thermal and electrical conductivities, low thermal expansion coefficients, chemical inertness, wear and oxidation resistance, and high thermal stability [1]. Group IVB diborides are currently employed in specialised applications, such as impact resistant armours, cutting tools, wear resistant coatings, molten metal crucibles, high temperature electrodes, and refractories for high-temperature manufacturing processes. Group IVB diborides are also potential candidates for the development of materials that can withstand ultra-high temperatures and extreme environments [2–4].

TiB_2, ZrB_2, and HfB_2 possess a hexagonal AlB_2-type crystal structure (space group P6/mmm, number 191), which can be depicted as honeycomb layers of boron separated by hexagonal closed-packed transition metal layers. The unit cell parameters of metal diborides can be attributed to the interatomic bond lengths of B–B and M–B bonds [5]. The length of the *a*-axis is primarily determined by the strength of covalent B–B bonds, and minimal changes in the *a*-axis are observed when different metal atoms are applied. However, cohesive forces in the *c*-direction are primarily due to M–B contacts, which increase with an increase in the M/B radius ratio and promote large changes in the *c*-axis.

When the differences in the atomic radii of metals are not extremely large, complete solid solubility occurs readily in isomorphous transition metal diborides due to the ability of the AlB_2-type structure to host a wide variety of metals along the *c*-direction. Thus, interest in diboride solid solutions would increase if their physical, chemical, or structural properties could be improved by controlling their stoichiometry. For example, Paderno et al. [6] have shown that the lattice parameters and B–B distance of the diboride phase of $(Ti, Zr)B_2$ solid solutions can be adjusted, which improves the perfectness and number of regularities in the microstructure of directionally crystallised MeB_6–MeB_2 eutectic composites. Mroz [7] demonstrated that $(Ti, Zr)B_2$ solid solutions exhibited increased mechanical properties (parabolic relationship) compared to those of end-member compositions. Moreover, in a previous study [8], a TiB_2–TaB_2 solid solution was formed to limit TiB_2 grain growth in ceramic matrix

* Corresponding author.
E-mail address: fgotor@cica.es (F.J. Gotor).

0272-8842/$36.00
doi:10.1016/j.ceramint.2011.02.004

composites and improve the mechanical properties of the materials.

Despite the scientific and technological interest in the formation of solid solutions, few studies have focused on reliable syntheses [9–13], and only restricted compositions have been evaluated. Nevertheless, some authors have reported the formation of solid solutions during the high-temperature processing of composite materials, including two different transition metal diborides [14–16]. However, due to the high refractoriness of these compounds, the materials are difficult to manufacture. Specifically, most of the proposed synthetic methods are characterised by high energetic requirements and are not suitable for the production of solid solutions.

The refractoriness and high stability of transition metal diborides are due to the high negative Gibbs free energy of formation, which is strongly correlated to the enthalpy of formation. Therefore, the synthesis of these compounds from a mixture of elements is an extremely exothermic process, and combustion-like methods can be employed as a practical means for their production. For instance, TiB_2, ZrB_2, and HfB_2 can be obtained by self-propagating high-temperature synthesis (SHS) [17–20]. Mechanochemical processes referred to as mechanically induced self-sustaining reactions (MSR) [21] are similar to thermally ignited SHS methods and also require highly exothermic chemical reactions [22]. Thus, the formation of TiB_2, ZrB_2, and HfB_2 by milling mixtures of elemental powders occurs through MSR [23,24].

MSR is a simple, low-energy procedure that produces a fine, homogeneous powder. With MSR, complex solid solutions can be obtained in a consistent and easy manner, and the chemical composition and microstructure of the materials can be controlled [25,26]. In a recent study [27], we demonstrated that ZrB_2–HfB_2 solid solutions could be synthesised by milling powder blends of hafnium, zirconium, and boron under an inert atmosphere. In the present investigation, MSR was used to obtain TiB_2–ZrB_2 and TiB_2–HfB_2 solid solutions, which present larger differences in atomic radii than that of ZrB_2–HfB_2. Moreover, the compositional range of each ternary system was investigated.

2. Material and methods

Titanium powder (99% pure, <325 mesh, Strem Chemicals, Newburyport, MA, USA), zirconium powder (<325 mesh, Alfa Aesar, Ward Hill, MA, USA), hafnium powder (99.6% pure, <325 mesh, Alfa Aesar, Ward Hill, MA, USA), and boron powder (95–97% pure, amorphous powder, Fluka, St. Louis, MO, USA) were used to synthesise the solid solutions.

A modified planetary ball-mill (model Micro Mill Pulverisette 7, Fritsch, Idar-Oberstein, Germany) was operated at a constant pressure by connecting the vial to a gas cylinder via a rotating union (model 1005-163-038, Deublin, Waukegan, IL, USA) and a flexible polyamide tube. In each milling experiment, 5 g of the powdered mixture and 7 tempered steel balls (d = 15 mm, m = 12.39 g) were placed in a 45-mL tempered steel vial (67 Rc) and were ball-milled under 6 bars of high-purity helium gas (H_2O < 3 ppm, O_2 < 2 ppm, and CnHm < 0.5 ppm, Air Liquide, Paris, France). The vial was purged with helium several times, and the pressure was selected prior to milling. The powder-to-ball mass ratio (PBR) was set to 1/17.35, and a spinning rate of 600 rpm was employed.

The occurrence of ignition during milling (a MSR process) was ascertained by monitoring the pressure of helium with an SMC solenoid valve (model EVT307-5DO-01F-Q, SMC Co., Tokyo, Japan). At ignition, the exothermic reaction provokes an instantaneous increase in the total pressure of the system due to an increase in the temperature. Thus, the ignition time (t_{ig}) of the mixtures was obtained from the time–pressure record. After ignition, milling was continued for 30 min to obtain a homogeneous product.

X-ray powder diffraction diagrams were obtained with a Philips X'Pert Pro instrument (Eindhoven, The Netherlands) equipped with a θ/θ goniometer, Cu Kα radiation (40 kV, 40 mA), a secondary K_β filter, and an X'Celerator detector. The diffraction diagrams were scanned from 20° to 150° (2θ) and 48° to 73.5° (2θ) in step-scan mode at a step of 0.017° and a counting time of 175 s/step and 2742 s/step, respectively. *In situ* high-temperature X-ray powder diffraction diagrams were recorded on the aforementioned instrument, which was equipped with an Anton Parr high-temperature attachment (HTK 1200). The diffraction patterns were obtained under a flow of helium at temperature intervals of 50 °C, and a maximum temperature of 1150 °C was investigated. The heating rate was set to 5 °C/min, and a scanning rate of 5.4° min^{-1} was applied. In total, the 2θ range was scanned from 20° to 80° for 12 min and 18 s.

Using the FULLPROF computer program, the lattice parameters were calculated from the peaks in the XRD diagram by assuming hexagonal symmetry [28]. The Williamson–Hall method [29] was used to separate the effects of domain size and microstrain on line broadening. The method assumes that the following mathematical relationship between the integral breadth (β), the size of the coherent crystalline domain (D), and the lattice distortion or microstrain (e) is applicable:

$$\frac{\beta\cos\theta}{\lambda} = \frac{1}{D} + 2e\left(\frac{2\sin\theta}{\lambda}\right)$$

A plot of $\beta\cos\theta/\lambda$ versus $2\sin\theta/\lambda$ was constructed, and the microstrain and the domain size were obtained from the slope and the intercept, respectively.

Transmission electron microscopy (TEM), electron diffraction (ED), and energy dispersive X-ray (EDX) experiments were performed on a 200 kV Philips CM-200 microscope (Eindhoven, The Netherlands) equipped with a supertwin objective lens, a LaB_6 filament, a ±45 tilt side-entry specimen holder (point resolution = 0.24 nm), and an EDS detector (EDAX Inc., Mahwah, NJ, USA). Powder samples were dispersed in ethanol and were deposited onto a holey carbon grid.

To study the thermal stability of the solid solutions, pellets of the milled samples were preformed by uniaxial pressing (12 MPa) and were annealed in a vertical tube furnace (Severn Furnaces Ltd., Bristol, England) at 1300 °C for 2 h (heating rate

Table 1
Mixtures submitted to milling and the corresponding ignition times (t_{ig}) and lattice parameters (a and c) of the AlB_2-type structure of TiB_2–ZrB_2 solid solutions after MSR.

Sample	Initial powder mixtures (elemental atomic ratio)	t_{ig} (min)	$a = b$ (Å)	c (Å)	c/a
Zr100	Zr/B (1/2)	113	3.1682(9)	3.5284(9)	1.114
Ti25Zr75	Ti/Zr/B (0.25/0.75/2)	120	3.1391(8)	3.4755(7)	1.107
Ti50Zr50	Ti/Zr/B (0.5/0.5/2)	143	3.1057(9)	3.4054(1)	1.096
Ti75Zr25	Ti/Zr/B (0.75/0.25/2)	97	3.0654(7)	3.3182(4)	1.082
Ti100	Ti/B (1/2)	47	3.0316(8)	3.2301(8)	1.065

10 °C/min, free cooling) in a flowing reductive H_2/He atmosphere (20/80) to prevent oxidation.

3. Results and discussion

3.1. TiB_2–ZrB_2 system

Table 1 shows the composition of the powder blends (Ti/Zr/B mixtures) submitted to high-energy ball milling for the synthesis of $Ti_{1-x}Zr_xB_2$ solid solution phases ($x = 0$, 0.25, 0.5, 0.75, and 1). The samples were labelled according to the nominal composition of the transition metals. For all of the mixtures, the time–pressure record, which was monitored during milling, confirmed the occurrence of mechanically induced self-sustaining reactions (MSR), and the corresponding ignition times (t_{ig}) are shown in Table 1. The t_{ig} values were not a linear function of the initial composition of the mixture (Table 1). In fact, the t_{ig} values of three-component mixtures were greater than the weighted average of the corresponding Ti/B and Zr/B binary mixtures, and Ti50Zr50 presented the maximum t_{ig} value. The results suggested that a mixture of Ti and Zr was more difficult to ignite than a mixture containing only one transition metal.

The XRD diagrams of the products revealed that the reactants were completely converted into a hexagonal diboride phase that could be described as a $Ti_{1-x}Zr_xB_2$ solid solution (Fig. 1). The weak reflection in some of the diagrams at 30.3° 2θ

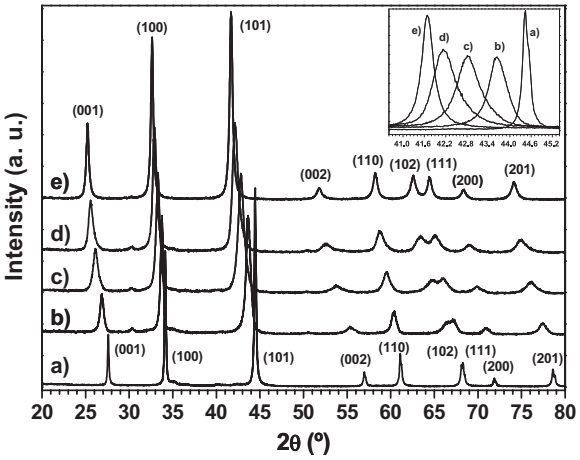

Fig. 1. X-ray powder diffraction diagrams of products obtained via the MSR of milled mixtures: (a) Ti100, (b) Ti75Zr25, (c) Ti50Zr50, (d) Ti25Zr75, and (e) Zr100. A hexagonal AlB_2-type structure was observed in all of the samples. In the inset, the (1 0 1) reflection is shown.

was attributed to the presence of tetragonal ZrO_2. The observed shift in the XRD reflections (see the (1 0 1) peak in the inset of Fig. 1) suggested that the chemical composition (Ti/Zr atomic ratio) of the solid solution was altered, which induced changes in the lattice parameters of the hexagonal structure. Using the FULLPROF program, the lattice parameters (a and c) were calculated from the XRD diagram (20–130°; 21 peaks) by assuming a P6/mmm hexagonal symmetry (Table 1). The lattice parameters for Ti100 and Zr100 were in good agreement with the theoretical values of TiB_2 and ZrB_2, respectively, and the ternary phases were between the aforementioned values, confirming the formation of TiB_2–ZrB_2 solid solutions. Moreover, the dependence of the lattice parameters on the nominal chemical composition was fairly linear, which suggested that the chemical composition of the solid solutions was similar to the stoichiometry of the initial mixture.

A careful examination of Fig. 1 revealed that the XRD diagrams of the ternary $Ti_{1-x}Zr_xB_2$ compounds featured broad reflections. Moreover, differences between the reflections of Zr100 and Ti100 were attributed to differences in the molar quantities of the MSR process. An important parameter that determines the milling intensity of a given process is the powder-to-ball mass ratio (PBR). Thus, when a set of experiments involving different systems are compared, the PBR must be held constant [21,30]. In the present study, we employed the same powder charge (5 g) and PBR ratio (1/17.35) in all of the milling experiments; therefore, the molar quantities were not normalised. When identical powder charges were employed and the enthalpies of formation (−315.9 kJ/mol and −323.8 kJ/mol for TiB_2 and ZrB_2, respectively) were similar, the heat generated in the MSR process leading to the formation of TiB_2 was approximately 1.6 times greater than the heat generated in the formation of ZrB_2. As a result, the crystallinity of TiB_2 was greater than that of ZrB_2.

The Williamson–Hall (WH) method was employed to estimate the size and microstrain of the materials. However, the WH plot of TiB_2, ZrB_2, and $Ti_{1-x}Zr_xB_2$ showed significant line broadening anisotropy (Fig. 2). For all of the samples, the nature of the line broadening was similar (only three of the plots are shown in Fig. 2), and the {0 0 l} reflections presented greater broadening than the {h k 0} reflections. Due to the dependence of the results on the {h k l} values, the WH method was applied to three different directions containing reflections with higher available orders, including (0 0 1) and (0 0 2), (1 0 0) and (2 0 0), and (1 0 1) and (2 0 2), respectively. The domain size and microstrain obtained from these directions are shown in Table 2.

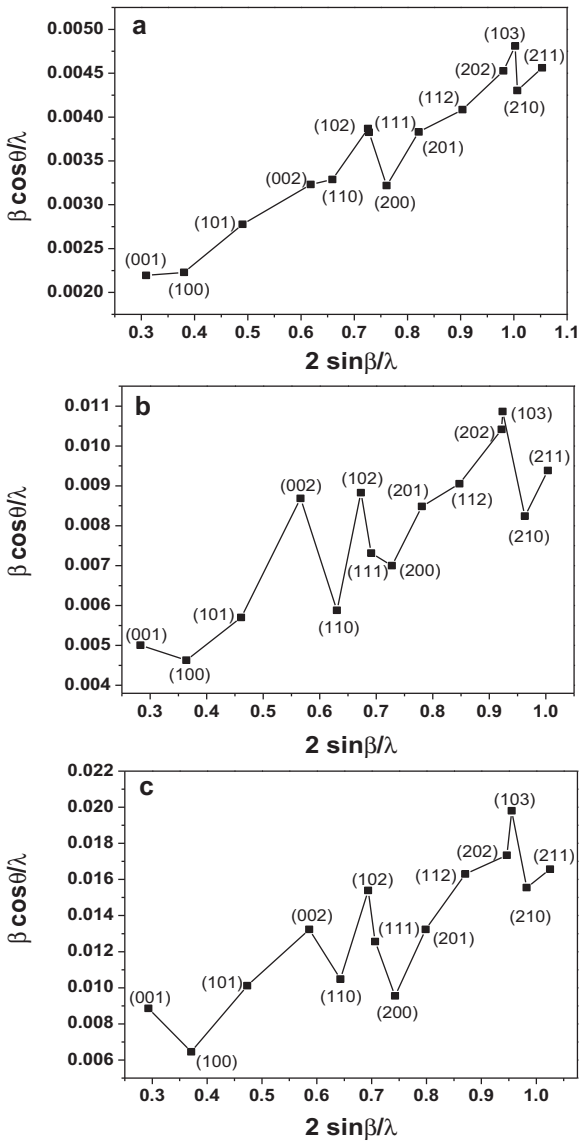

Fig. 2. Williamson–Hall plots of: (a) Ti100, (b) Zr100, and (c) Ti50Zr50, which show significant line-broadening anisotropy.

Clear trends in the values presented in Table 2 were observed. First, the ternary phases ($Ti_{1-x}Zr_xB_2$ $(0 < x < 1)$) possessed smaller diffracting domains (in the nanometric range) than the binary phases (TiB_2 and ZrB_2). The presence of Zr and Ti in the initial mixture delayed the ignition of the self-sustained reaction and reduced grain growth during the MSR process. Second, the dependence of line broadening anisotropy on microstrain was greater than that of the diffracting domain size. Similar crystallite sizes were obtained for the three family planes; however, the lattice microstrain of the $\{h\,0\,0\}$ diffraction planes was significantly lower than that of the other directions. This microstrain anisotropy may be due to the crystal structure of the diborides, which are characterised by basal planes with strong covalent B–B bonds that hinder an increase in this direction. However, hindrance along the *c*-direction was not observed because the cohesive forces were lower; and defects introduced into the material during the MSR process can be easily accommodated along this direction. Finally, the results shown in Fig. 2 and Table 2 indicated that the most crystalline sample (Ti100) presented less microstrain and reduced anisotropy.

Table 2
Diffracting domain size (*D*) and microstrain (*e*), which were calculated by the Williamson–Hall method for three different family planes.

Sample	(*h k l*)	*D* (nm)	*e* (%)
Zr100	(0 01)–(0 0 2)	75	0.65
	(1 0 0)–(2 0 0)	67	0.38
	(1 0 1)–(2 0 2)	83	0.49
Zr75Ti25	(0 0 1)–(0 0 2)	28	0.71
	(1 0 0)–(2 0 0)	34	0.39
	(1 0 1)–(2 0 2)	37	0.68
Zr50Ti50	(0 0 1)–(0 0 2)	22	0.75
	(1 0 0)–(2 0 0)	30	0.42
	(1 0 1)–(2 0 2)	34	0.76
Zr25Ti75	(0 0 1)–(0 0 2)	42	0.68
	(1 0 0)–(2 0 0)	48	0.34
	(1 0 1)–(2 0 2)	56	0.62
Ti100	(0 0 1)–(0 0 2)	86	0.17
	(1 0 0)–(2 0 0)	81	0.13
	(1 0 1)–(2 0 2)	97	0.18

Fluctuations in the lattice spacing (due to chemical inhomogeneities) are dependent on the crystallographic

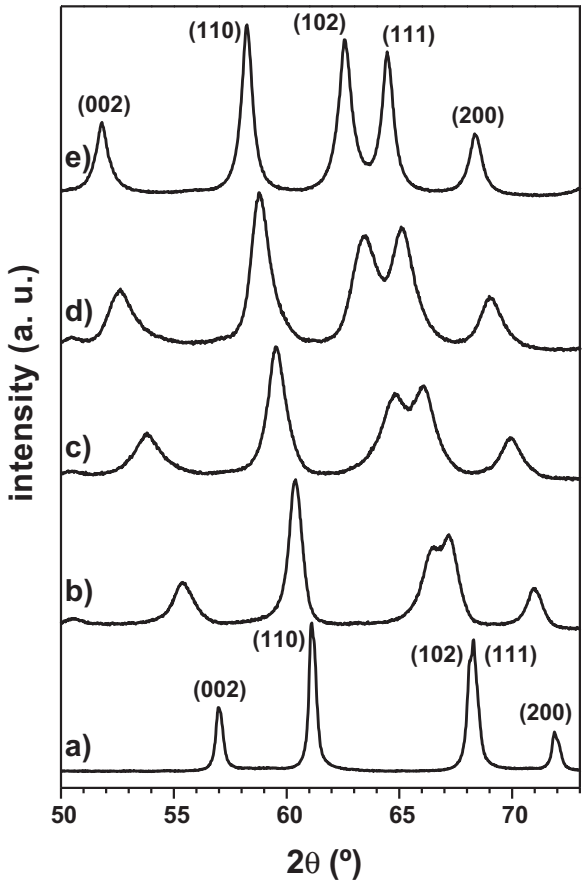

Fig. 3. X-ray powder diffraction diagrams of products obtained via MSR. The diffractograms depict the TiB_2–ZrB_2 system in the angular range, including (0 0 2), (1 1 0), (1 0 2), (1 1 1), and (2 0 0) reflections in the AlB_2-type structure. (a) Ti100, (b) Ti75Zr25, (c) Ti50Zr50, (d) Ti25Zr75, and (e) Zr100.

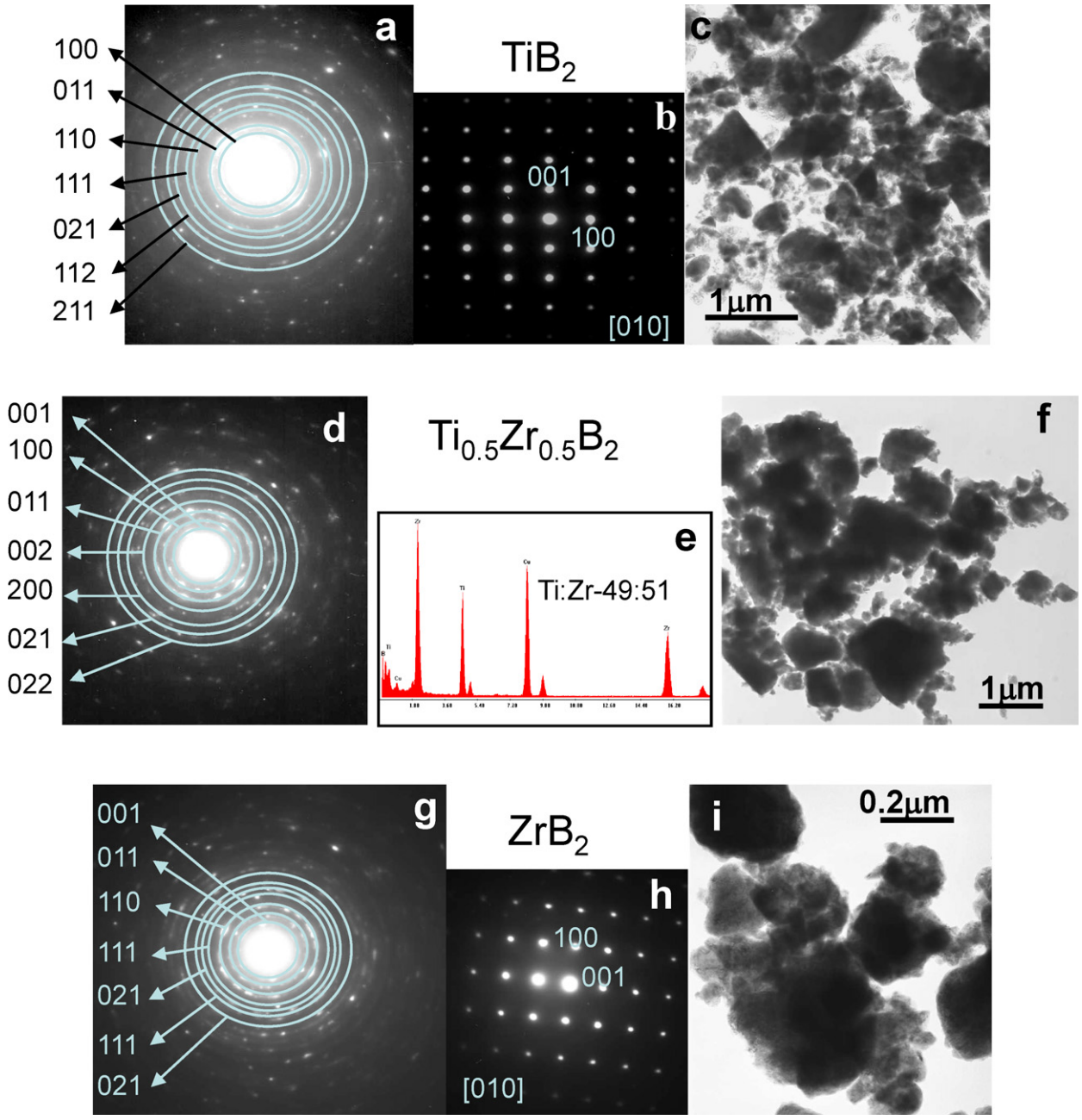

Fig. 4. TEM, ED, and EDX results of the diboride phases: (a–c) T100, (d–f) Ti50Zr50, and (g–i) Zr100.

direction; thus, the existence of compositional heterogeneities in $Ti_{1-x}Zr_xB_2$ solid solutions may also induce large and anisotropic broadening in the XRD reflections. Specifically, greater broadening would be observed when the *d*-spacings of TiB_2 and ZrB_2 are highly divergent. To determine if XRD line broadening anisotropy was due to chemical heterogeneities, XRD diagrams were recorded at an extremely low speed between 48° and 73.5° (2θ), where the (0 0 2), (1 1 0), (1 0 2), (1 1 1), and (2 0 0) peaks of the AlB_2-type structure are observed (Fig. 3). This angular range is useful because (0 0 2), (1 1 0), and (2 0 0) reflections in TiB_2 and ZrB_2 differ by 5.25°, 2.92°, and 3.60°, respectively. In contrast, (1 0 2) and (1 1 1) reflections overlap in TiB_2 and are separated by 1.89° in ZrB_2. A careful analysis of the XRD diagrams shown in Fig. 3 revealed that line broadening anisotropy in the binary and ternary phases was similar, and (0 0 l), (*h k* 0), and the other (*h k l*) indexes were differentiated for all of the solid solutions. Therefore, $Ti_{1-x}Zr_xB_2$ samples obtained by MSR can be considered homogeneous from a stoichiometric point of view.

To substantiate the aforementioned results and to obtain more detailed information on the microstructure of the samples, transmission electron microscopy techniques were conducted (TEM, ED and EDX), and a summary of the results is presented in Fig. 4. For the sake of simplicity, only the results corresponding to Ti100 (Fig. 4a–c), Ti50Zr50 (Fig. 4d–f), and Zr100 (Fig. 4g–i) are shown. TEM micrographs confirmed that the samples were similar from a morphological point of view, and particles formed by the aggregation of small

Table 3
Mixtures submitted to milling and the corresponding ignition times (t_{ig}) and lattice parameters (a and c) of the AlB_2-type structure of TiB_2–HfB_2 solid solutions after MSR.

Sample	Initial powder mixtures (elemental atomic ratio)	t_{ig} (min)	$a = b$ (Å)	c (Å)	c/a
Hf100	Hf/B (1/2)	27	3.1458(6)	3.4778(9)	1.106
Ti25Hf75	Ti/Hf/B (0.25/0.75/2)	30	3.1250(6)	3.4393(3)	1.101
Ti50Hf50	Ti/Hf/B (0.5/0.5/2)	40	3.0955(2)	3.3731(6)	1.090
Ti75Hf25	Ti/Hf/B (0.75/0.25/2)	52	3.0533(7)[a]	3.2805(8)[a]	1.074[a]
Ti100	Ti/B (1/2)	47	3.0316(8)	3.2301(8)	1.065

[a] Lattice parameters correspond to the main phase observed in the XRD diagram.

crystallites were observed (Fig. 4c, f, and i). As shown in the micrographs, the diffraction domain size of the materials was significantly dispersed. Moreover, smaller crystallites were rounder than larger crystallites, which presented a platelet-like shape. The electron diffraction study results revealed that the majority of the crystallites in the binary phases (Ti100 and Zr100) were between 50 and 100 nm. Although these samples showed ring-ED patterns (Fig. 4a and g), larger crystals (next to 300 nm) were also observed, leading to dot-ED patterns (as shown in Fig. 4b and h). However, only ring-ED patterns were obtained in the ED study of the ternary phases in the TiB_2–ZrB_2 system (Fig. 4d); thus, the average crystallite size was slightly smaller than that of the binary phases.

EDX analyses were performed on the ternary phases ($Ti_{1-x}Zr_xB_2$ with $x = 0.25$, 0.5, and 0.75), and the results shown in Fig. 4e correspond to the $x = 0.5$ phase. Although the composition of individual crystallites was not exactly the same (a few crystallites contained larger quantities of Ti or Zr), the composition of most particles (Ti:Zr = 49:51) suggested that the Ti/Zr atomic ratio was similar to that of the nominal starting composition.

3.2. TiB_2–HfB_2 system

Another set of milling experiments was performed to obtain TiB_2–HfB_2 solid solution phases (Table 3). In this system, MSR always occurred, and the ignition times for the milled mixtures are shown in Table 3. Similar to the results of the previously described experiments, a tendency toward longer ignition times was observed when ternary mixtures were milled. However, in the TiB_2–HfB_2 system, the trend was less significant because TiB_2 and HfB_2 end-members possessed similar t_{ig} values.

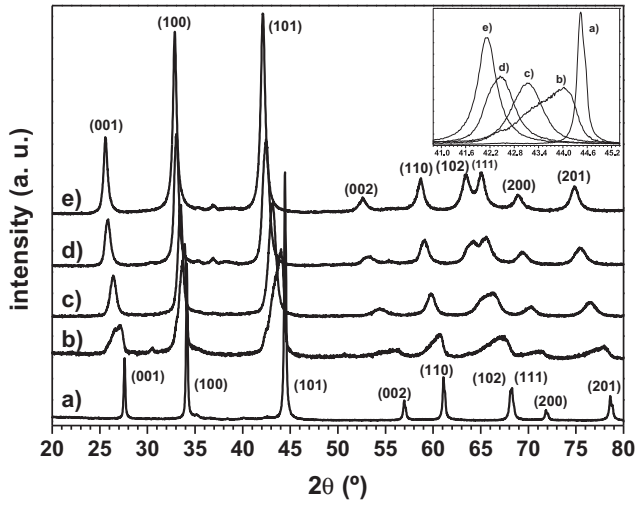

Fig. 5. X-ray powder diffraction diagrams of products obtained via the MSR of milled mixtures: (a) Ti100, (b) Ti75Hf25, (c) Ti50Hf50, (d) Ti25Hf75, and (e) Hf100. In the inset, the (1 0 1) reflection is shown.

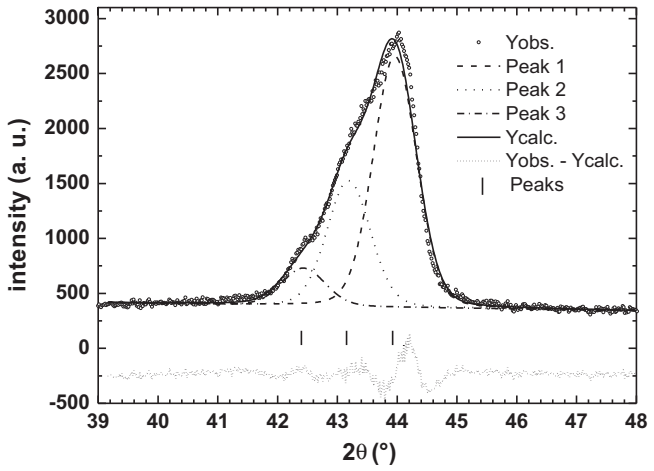

Fig. 6. Deconvolution of the (1 0 1) reflection of the product obtained after the MSR of Ti75Hf25. Three different phases were present in the $Ti_{1-x}Hf_xB_2$ solid solution.

The XRD patterns of the products (Fig. 5) revealed that AlB_2-type diboride phases that can be described as solid solutions with the formula $Ti_{1-x}Hf_xB_2$ formed under the reaction conditions. In Ti75Hf25, a chemically homogeneous phase was not produced, as revealed by the asymmetry of the XRD lines. Thus, the XRD reflections of Ti75Hf25 were deconvoluted by assuming that at least three different phases in the $Ti_{1-x}Hf_xB_2$ solid solution contained different chemical

Table 4
Diffracting domain size (D) and microstrain (e), which were calculated according to the Williamson–Hall method for three different family planes.

Sample	(h k l)	D (nm)	e (%)
Hf100	(0 0 1)–(0 0 2)	20	0.37
	(1 0 0)–(2 0 0)	18	0.18
	(1 0 1)–(2 0 2)	26	0.41
Hf75Ti25	(0 0 1)–(0 0 2)	29	0.95
	(1 0 0)–(2 0 0)	22	0.49
	(1 0 1)–(2 0 2)	40	0.82
Hf50Ti50	(0 0 1)–(0 0 2)	31	0.60
	(1 0 0)–(2 0 0)	26	0.34
	(1 0 1)–(2 0 2)	39	0.63

compositions (different x values) (Fig. 6). The stoichiometry of the most abundant phase was slightly richer in Ti than the initial nominal composition, and the two minor phases possessed chemical compositions that were similar to those of Ti50Hf50 and Ti25Hf75. The difficulty associated with the production of homogeneous phases at high Ti contents is in contrast with the

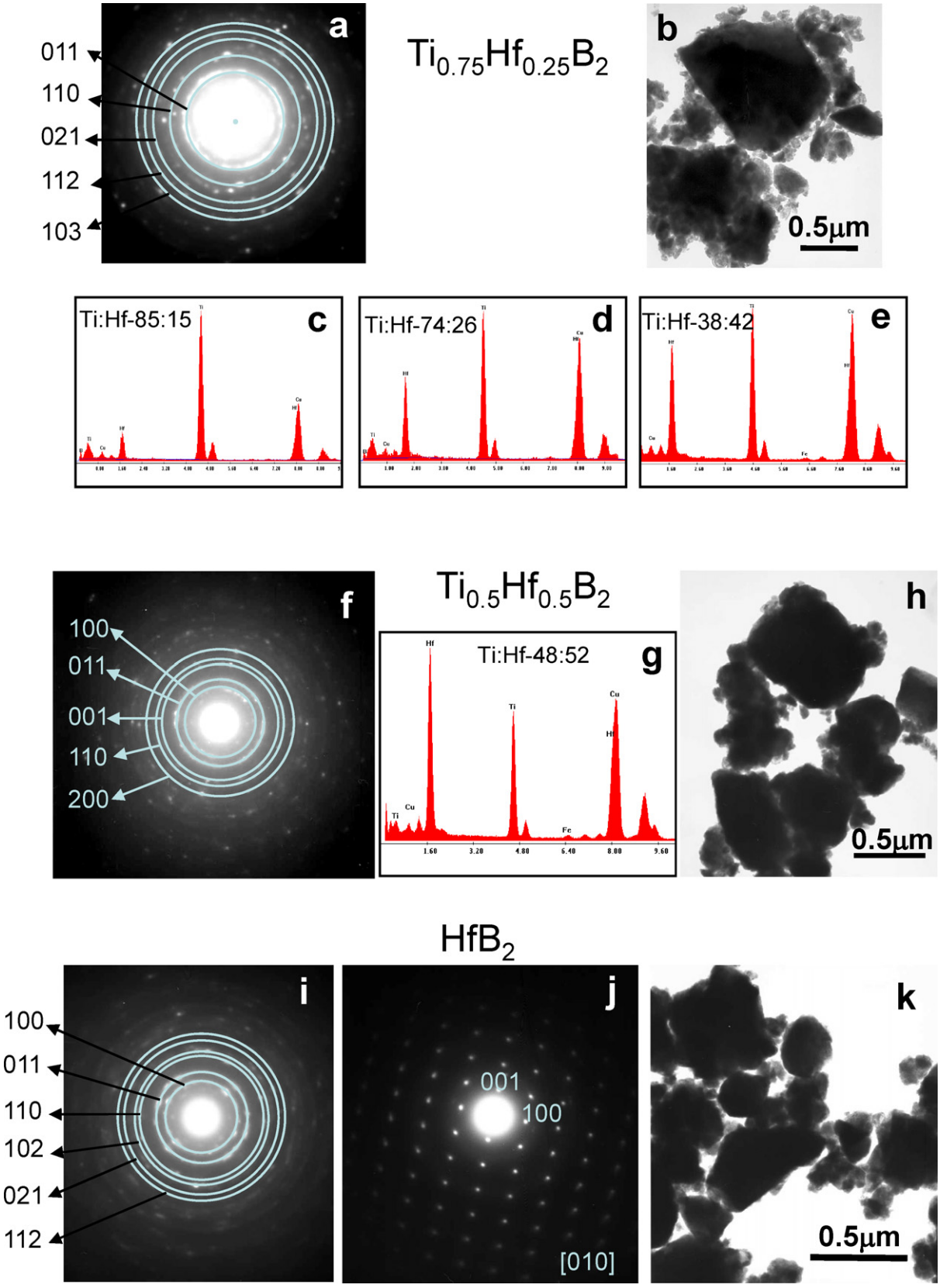

Fig. 7. TEM, ED, and EDX results of the diboride phases of: (a–e) T75Hf25, (f–h) Ti50Hf50, and (i–k) Hf100.

results observed in the TiB_2–ZrB_2 system, where unlimited solid solubility was achieved. This behaviour is not related to the large disparity in the size of Hf and Ti atoms because Zr has a larger radius than Hf in the AlB_2-structure.

The lattice parameters (a and c) of the TiB_2–HfB_2 system were also determined and are shown in Table 3. For Ti75Hf25, only the major phase was considered in the calculation. Similar to the previous system, the lattice parameters were almost linearly dependent on the nominal chemical composition. As expected, only minor deviations from this dependence were observed for the main phase in Ti75Hf25 due to the presence of other phases with higher Hf contents. These results again confirm that the stoichiometry of the solid solution was controlled by adjusting the initial chemical composition of the elemental mixture.

The XRD line profile shown in Fig. 5 revealed broad reflections and anisotropic broadening, which were also observed in the previous system. Significant broadening in samples containing Hf was related to the generation of lower quantities of heat in the MSR process. The same powder charge (5 g) and PBR ratio (1/17.35) was maintained in the TiB_2–HfB_2 system; thus, the heat released during MSR leading to HfB_2 was 2.8 and 1.7 times lower than the heat evolved during the formation of TiB_2 and ZrB_2, respectively. Due to the anisotropic broadening of XRD reflections, the diffracting domain size and microstrain of planes with multiple orders were calculated. The results obtained from mixtures leading to chemically homogeneous samples confirmed the nanometric character of the solid solution; thus, microstrain was the origin of anisotropic broadening in the XRD diagrams (Table 4).

Structural and microstructural characterisation by TEM-related techniques corroborated the aforementioned results, and a resume of the TiB_2–HfB_2 system is presented in Fig. 7 (Ti75Hf25, Ti50Hf50, and Hf100). The results for Ti100 were previously presented (Fig. 4). As shown in the figures, the micrographs confirmed that the samples possessed similar microstructures, which were characterised by large particles formed by the aggregation of small crystallites (Fig. 7b, h, and k). In the electron diffraction study, dot-ED diagrams were only obtained for the binary phase (Hf100) (Fig. 7j). However the majority of ED results showed ring-ED patterns, indicating that the crystallite sizes were between 50 and 100 nm (Fig. 7a, f, and i).

The three ternary phases ($Ti_{1-x}Hf_xB_2$ with $x = 0.25$, 0.5, and 0.75) were analysed by EDX. Minor deviations in the nominal composition were observed for Ti50Hf50 and Ti25Hf75, and a representative average spectrum for Ti50Hf50 is presented in Fig. 7g. Alternatively, the results for Ti75Hf25 were quite different. Although the average atomic ratio of Ti/Zr was similar to the nominal composition (Fig. 7d, Ti:Hf = 74:26), many regions with higher concentrations of Ti or Hf were observed (Fig. 7c and e). These results agree with those obtained by XRD, confirming that Ti75Hf25 was formed by at least three different phases.

3.3. Thermal stability of $Ti_{1-x}Zr_xB_2$ and $Ti_{1-x}Hf_xB_2$

To investigate the thermal stability of $Ti_{1-x}Zr_xB_2$ and $Ti_{1-x}Hf_xB_2$ solid solutions, samples synthesised by MSR were pressed to form pellets and were annealed at 1300 °C for 2 h in a reductive atmosphere (He/H_2) to prevent oxidation. The samples were characterised by XRD (Fig. 8), and the results revealed that significant phase separation and changes in the chemical composition of the solid solutions did not occur.

Powder materials obtained by milling processes frequently show high reactivity due to a large number of defects and a high interface area. In general, milled powders require lower sintering temperatures and are more sensitive to undesirable processes such as oxidation. As an example, this phenomenon was confirmed for Ti25Zr75. Fig. 9 shows the experimental XRD results as a function of the temperature under a flow of helium and a low partial pressure of oxygen, which allows oxidation to occur.

As shown in Fig. 9, the oxidation of the solid solution began at 750 °C and progressed continuously as the temperature increased. Moreover, between 850 °C and 950 °C, the metastable tetragonal ZrO_2 structure was transformed into a stable monoclinic phase. An XRD diagram was also obtained upon cooling the partially oxidised sample, and the reflections corresponding to the monoclinic oxide phase were shifted toward higher 2θ angles compared to the reference pattern (PDF

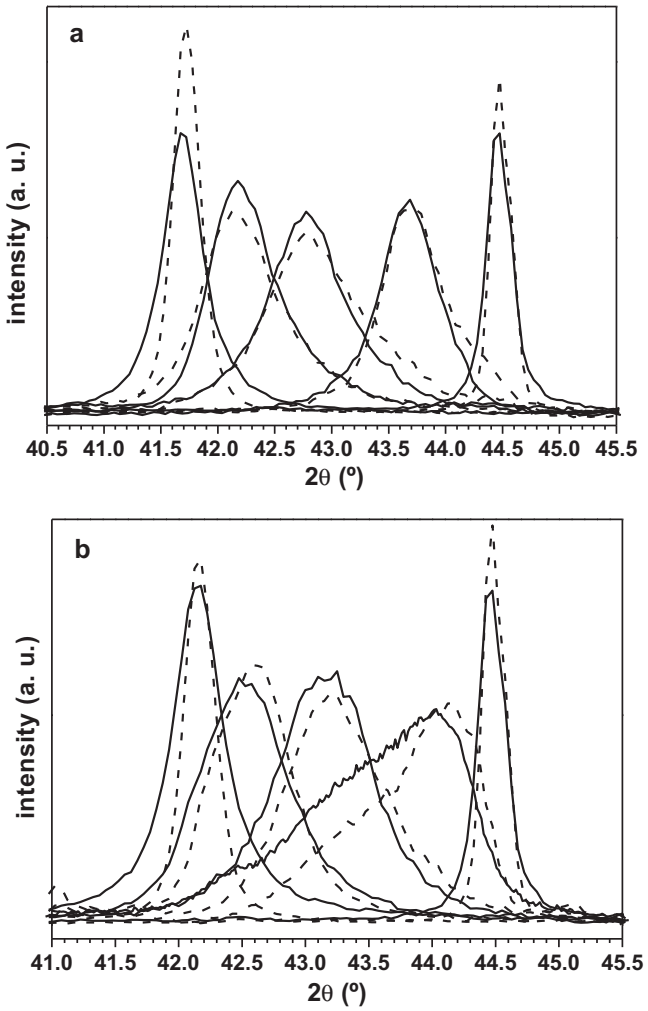

Fig. 8. X-ray powder diffraction results of the (1 0 1) reflection after MSR (—) and annealing at 1300 °C (···): (a) TiB_2–ZrB_2 and (b) TiB_2–HfB_2 systems.

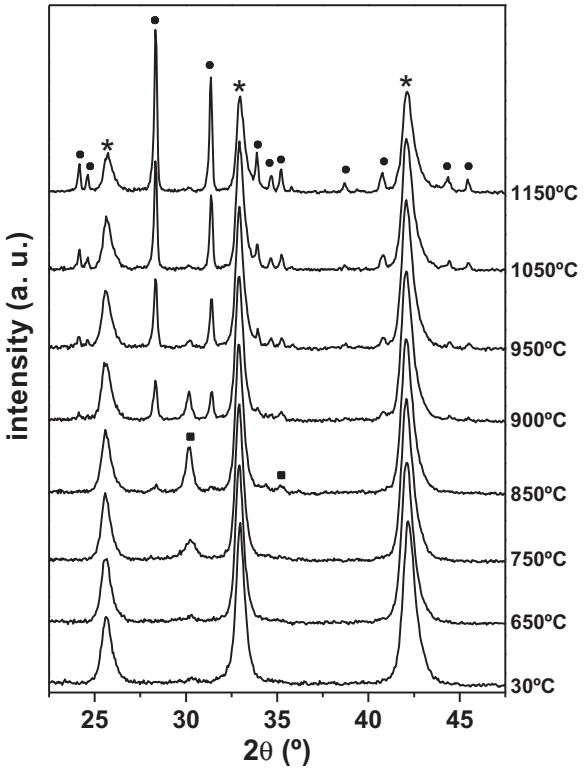

Fig. 9. Thermal evolution of the XRD pattern of Ti25Zr75 under low partial pressures of oxygen at an overall pressure of 1 atm (helium was used as the carrier gas): (*) $Ti_{0.25}Zr_{0.75}B_2$; (•) *m*-ZrO_2; (■) *t*-ZrO_2.

37-1484). These results indicated that Ti was present in the monoclinic structure. Moreover, the presence of Ti was further supported by the fact that a titanium oxide phase was not detected in the oxidised sample.

4. Conclusions

$Ti_{1-x}Zr_xB_2$ and $Ti_{1-x}Hf_xB_2$ solid solutions were obtained by high-energy ball-milling elemental mixtures (Ti/Zr/B and Ti/Hf/B, respectively) under an inert atmosphere. For all of the samples, mechanically induced self-sustaining reactions (MSR) were observed, and the ignition times were dependent on the initial composition of the mixture. The stoichiometry of the solid solutions was controlled by adjusting the atomic ratio of the elements in the reactant mixture, and the entire compositional range of the TiB_2–ZrB_2 system could be obtained via MSR. Moreover, a single phase (one term in the solid solution) was produced for each ternary Ti/Zr/B reactant mixture. In the TiB_2–HfB_2 system, solid solutions with good chemical homogeneity were observed, except for reactant mixtures rich in Ti, which provided inhomogeneous products consisting of a mixture of different terms in the solid solution.

In both systems, the dependence of the lattice parameters on the chemical composition was linear. The thermal stability of the solid solutions was ascertained by high-temperature isothermal annealing at 1300 °C, indicating that the materials could be used as raw materials in the development of technological composites. However, the solid solutions were highly reactive due to the large number of defects introduced into the structure by the milling process; thus, these compounds must be carefully processed to avoid oxidation.

Acknowledgments

This work was supported by the Spanish government under grant No. MAT2006-04911 and MAT2010-17046. The grants were financed in part by the European Regional Development Fund 2007-2013. The authors wish to thank Ms. C. Gallardo for her assistance in high-energy ball-milling experiments.

References

[1] R. Telle, L.S. Sigl, K. Takagi, Boride-based hard materials, in: R. Riedel (Ed.), Handbook of Ceramic Hard Materials, vol. 2, Wiley-VCH, Weinheim, 2000, pp. 802–945.
[2] M.J. Gasch, D.T. Ellerby, S.M. Johnson, Ultra high temperature ceramic composites, in: N.P. Bansal (Ed.), Handbook of Ceramic Composites, Kluwer Academic Publisher, Boston, 2005, pp. 197–224.
[3] W.G. Fahrenholtz, G.E. Hilmas, I.G. Talmy, J.A. Zaykoski, Refractory diborides of zirconium and hafnium, J. Am. Ceram. Soc. 90 (2007) 1347–1364.
[4] T.H. Squire, J. Marschall, Material property requirements for analysis and design of UHTC components in hypersonic applications, J. Eur. Ceram. Soc. 30 (2010) 2239–2251.
[5] K.E. Spear, Chemical bonding in AlB_2-type borides, J. Less Common Metals 47 (1976) 195–201.
[6] Y. Paderno, V. Paderno, V. Filippov, Some peculiarities of eutectic crystallization of LaB_6–$(Ti,Zr)B_2$ alloys, J. Solid State Chem. 154 (2000) 165–167.
[7] C. Mroz, Processing TiZrC and $TiZrB_2$, Am. Ceram. Soc. Bull. 73 (1994) 78–81.
[8] V. Chauvel-Kokabi, K. Shobu, T Watanabe, Studies of the mechanical properties of TiB_2–6%TaB_2–1%CoB–*x*%mZrO_2, J. Eur. Ceram. Soc. 17 (1997) 885–890.
[9] S. Otani, T. Aizawa, N. Kieda, Solid solution ranges of zirconium diboride with other refractory diborides: HfB_2, TiB_2, TaB_2, NbB_2, VB_2, and CrB_2, J. Alloys Compd. 475 (2009) 273–275.
[10] B. Post, F.W. Glaser, D. Moskowitz, Transition metal diborides, Acta Metall. 2 (1954) 20–25.
[11] E.A. Knyshev, V.M. Novgorodtsev, U.S. Plyshevski, V.A. Kobyakov, Z.G. Stepanova, V.V. Svistunov, A.R. Becketov, Synthesis of transition metal borides and their properties, J. Less Common Metals 47 (1976) 273–278.
[12] J. Inagaki, Y. Sakai, N. Uekawa, T. Kojima, K. Kakegawa, Synthesis and evaluation of $Zr_{0.5}Ti_{0.5}B_2$ solid solution, Mater. Res. Bull. 42 (2007) 1019–1027.
[13] L. Rao, E.G. Gillan, R.B. Kaner, Rapid synthesis of transition metal borides by solid state metathesis, J. Mater. Res. 10 (1995) 353–361.
[14] F. Monteverde, A. Bellosi, S. Guicciardi, Processing and properties of zirconium diboride-based composites, J. Eur. Ceram. Soc. 22 (2002) 279–288.
[15] Y. Xie, T.H. Sanders Jr., R.F. Speyer, Solution-based synthesis of submicrometer ZrB_2 and ZrB_2–TaB_2, J. Am. Ceram. Soc. 91 (2008) 1469–1474.
[16] F. Monteverde, A. Bellosi, L. Scatteia, Processing and properties of ultra-high temperature ceramics for space applications, Mater. Sci. Eng. A 485 (2008) 415–421.
[17] A. Makino, C.K. Law, SHS combustion characteristics of several ceramics and intermetallic compounds, J. Am. Ceram. Soc. 77 (1994) 778–786.
[18] D.D. Radev, M. Marinov, Properties of titanium and zirconium diborides obtained by self-propagated high-temperature synthesis, J. Alloys Compd. 244 (1996) 48–51.

[19] H.E. Camurlu, F. Maglia, Preparation of nano-size ZrB_2 powder by self-propagating high-temperature synthesis, J. Eur. Ceram. Soc. 29 (2009) 1501–1506.
[20] S. Nakane, T. Endo, K. Hirota, Simultaneous synthesis and densification of alpha-Zr(N)/ZrB_2 composites by self-propagating high-temperature combustion under high nitrogen pressure, Ceram. Int. 35 (2009) 2145–2149.
[21] L. Takacs, Self-sustaining reactions induced by ball milling, Prog. Mater. Sci. 47 (2002) 355–414.
[22] J.M. Córdoba, M.J. Sayagués, M.D. Alcalá, F.J. Gotor, Monophasic nanostructured powders of niobium, tantalum, and hafnium carbonitrides synthesized by a mechanically induced self-propagating reaction, J. Am. Ceram. Soc. 90 (2007) 381–387.
[23] L. Takacs, Milling-induced combustion in powder mixtures containing titanium, zirconium, or hafnium, J. Solid State Chem. 125 (1996) 75–84.
[24] D.D. Radev, D. Klissurski, Mechanochemical synthesis and SHS of diborides of titanium and zirconium, J. Mater. Synth. Process. 9 (2001) 131–136.
[25] J.M. Córdoba, M.J. Sayagués, M.D. Alcalá, F.J. Gotor, Monophasic $Ti_yNb_{1-y}C_xN_{1-x}$ nanopowders obtained at room temperature by MSR, J. Mater. Chem. 17 (2007) 650–653.
[26] J.M. Córdoba, M.A. Avilés, M.J. Sayagués, M.D. Alcalá, F.J. Gotor, Synthesis of complex carbonitride powders $Ti_yMT_{1-y}C_xN_{1-x}$ (MT: Zr, V, Ta, Hf) via a mechanically induced self-sustaining reaction, J. Alloys Compd. 482 (2009) 349–355.
[27] M.A. Avilés, J.M. Córdoba, M.J. Sayagués, M.D. Alcalá, F.J. Gotor, Mechanosynthesis of $Hf_{1-x}Zr_xB_2$ solid solution and $Hf_{1-x}Zr_xB_2$/SiC composite powders, J. Am. Ceram. Soc. 93 (2010) 696–702.
[28] J. Rodriguez-Carvajal, Recent developments of the program FULLPROF, in Commision on Powder Diffraction (IUCr), Newsletter 26 (2001) 12–19.
[29] G.K Williamson, W.H. Hall, X-ray line broadening from filed aluminium and wolfram, Acta Metall. 1 (1953) 22–31.
[30] C. Suryanarayana, Mechanical alloying and milling, Prog. Mater. Sci. 46 (2001) 1–184.